

Analytic Solution of Stochastic Completion Fields

K. K. Thornber

L. R. Williams

NEC Research Institute
4 Independence Way
Princeton, NJ 08540

Abstract

We use generalized particle trajectories to derive an analytic expression characterizing the probability distribution of boundary-completion shape. This is essential to the understanding of the perceptual phenomenon of illusory (subjective) contours. The particles' dynamics include Poisson-distributed ensembles of driving forces as well as particle decay. The resulting field, representing completed surface boundaries, is characterized by the fraction of particles at \mathbf{x} with velocity $\dot{\mathbf{x}}$. The distributions are projectively covariant in the sense that fields calculated in any lower-dimensional projection correspond to the projections of fields calculated in any higher dimension. Being analytic, the relationship between velocity, diffusivity, and decay can be made readily apparent.

1 Introduction

The phenomenon of illusory contours is much studied by visual psychologists and provides a compelling example of human visual competence not yet demonstrated by computer vision systems. Recently, a novel theory of illusory contour shape and salience has appeared. Williams and Jacobs[11] defined the illusory contour shape and salience problem to be the problem of computing the the shape and relative likelihood (as determined by the prior probability distribution) of the family of curves which potentially connect (or complete) a set of contrast edges. Like Mumford[6], they proposed that the probability distribution can be modeled by a random walk in a space of positions and orientations. This random walk has the property that maximum likelihood paths are curves of least energy (i.e., the shape commonly assumed to model the shape of illusory contours[4]). In this paper, we use generalized particle trajectories to derive an analytic expression for this probability distribution,

which Williams and Jacobs call the *stochastic completion field*. Although the original treatment relied on Monte-Carlo methods to solve the non-linear stochastic differential equation defining the random walk, there are situations where Monte Carlo methods are inadequate. Low probability events can be unacceptably noisy for simulation times of practical length. Fortunately, an analytic solution is available, and this solution, while more general, has the additional virtues of being simpler and more efficient to compute. Most importantly, the analytic solution permits an analysis of properties of the distribution not previously possible (e.g. its expected value and variance). Being analytic, the relationship between velocity, diffusivity, and decay (all components of the original treatment) can be made readily apparent.

2 Prior Work

The earliest theory of illusory contour shape is due to Ullman[9]. Ullman hypothesized that the curve used by the human visual system to join two contour fragments is constructed from two circular arcs. Each circular arc is tangent to its sponsoring contour at one end and to the other arc at the point of intersection. From the family of possible curves of this form, the pair which minimizes total bending energy (i.e., $E = \int \kappa(s)^2 ds$) models the shape of the illusory contour. Ullman suggested that illusory contours could be computed in parallel in a network by means of local operations, but he never tested this idea.

More recently, Guy and Medioni[2] describe a method for computing a vector-field representing global image structure from local tangent measurements. The key to their approach is the local summation of a set of global voting patterns representing orientations which are co-circular to the tangent measurements. Consequently, the vector-field is non-stochastic (i.e., deterministic), and cannot model the prior distribution of completion shapes.

Heitger and von der Heydt[3] describe a theory of figural completion based upon non-linear combination of the convolutions of “keypoint” images with a fixed set of oriented grouping filters. Keypoints are located at negative minima or positive maxima of curvature (i.e., corners) in a luminance boundary and represent the pair of orientations at likely points of occlusion. Significantly, they demonstrate their method on both illusory contour figures

like the Kanizsa triangle and on more “realistic” images (e.g. of plants and rocks) with impressive results.

3 Approach

First picture a set of positions and velocities $\{\mathbf{x}_i, \dot{\mathbf{x}}_i\}$ in the image plane. These represent locations where one surface boundary occludes another. Following [3], these will be termed keypoints. Then consider the set $\{\mathbf{x}(t) \mid \{\mathbf{x}_i, \dot{\mathbf{x}}_i\}\}$ of all parameterized curves which pass from any \mathbf{x}_i to any \mathbf{x}_j (j can be i) with increasing t subject only to the restriction that whenever $\mathbf{x}(t) = \mathbf{x}_k$, $\partial_t \mathbf{x}(t) = \dot{\mathbf{x}}_k$.¹ We now ask the question: How can the distribution of curves which pass through the keypoints with these velocities be characterized? One way is to consider the trajectories of particles under the influence of random forces. Since both position and velocity are important, the treatment must go beyond simple diffusion. Consequently, characterization is more complex. We choose to focus on the fraction of particles at \mathbf{x} with some velocity $\dot{\mathbf{x}}$ (i.e., at each field point we have a distribution of velocities). The result is a stochastic field of tangents grounded in the set of keypoints $\{\mathbf{x}_i, \dot{\mathbf{x}}_i\}$.

4 Treatment

Given a distribution $\{\mathbf{x}_i\}$ of trajectories $\mathbf{x}(t)$, each constrained to pass through two keypoints, we wish to calculate the fraction of particles at all other points \mathbf{x} , with velocity $\dot{\mathbf{x}}$. Furthermore, we shall do the calculation in such a way that we shall also be able to determine joint velocity-velocity distributions, both pair-wise and higher order if necessary. The expressions will be analytic throughout, and reduce to relatively simple, calculatable forms in many realistic cases.

Suppose by $P(2, 3 \mid 1)$ we mean the probability that a particle, subject to some dynamics and various stochastic forces leaves \mathbf{x}_1 with velocity $\dot{\mathbf{x}}_1$ at time t_1 , is at \mathbf{x}_3 with $\dot{\mathbf{x}}_3$ at t_3 , and

¹Normally curves are parameterized in terms of distance s along them. However, then $|d\mathbf{x}/ds| = 1$, and we lose a degree of freedom (i.e., speed when the curves are particle trajectories). We will need this degree of freedom.

arrives at \mathbf{x}_2 with $\dot{\mathbf{x}}_2$ at t_2 such that $t_1 \leq t_3 \leq t_2$. If at \mathbf{x}_1 we have a source of such particles $I_1(t)$, then

$$\int_{-\infty}^{t_3} dt_1 P(2, 3 | 1) I_1(t_1) / \int_{-\infty}^{t_3} dt_1 P(2 | 1) I_1(t_1)$$

will be the fraction of those particles from the source arriving at \mathbf{x}_2 with $\dot{\mathbf{x}}_2$ at t_2 which are at \mathbf{x}_3 with $\dot{\mathbf{x}}_3$ at t_3 . If we weight the arrival times according to $J_2(t_2)$, then the fraction going from **1** ($\mathbf{x}_1, \dot{\mathbf{x}}_1$) to **2** ($\mathbf{x}_2, \dot{\mathbf{x}}_2$) which are at **3** ($\mathbf{x}_3, \dot{\mathbf{x}}_3$) is simply:

$$\int_{t_3}^{\infty} dt_2 \int_{-\infty}^{t_3} dt_1 P(2, 3 | 1) I_1(t_1) J_2(t_2) / \int_{t_3}^{\infty} dt_2 \int_{-\infty}^{t_3} dt_1 P(2 | 1) I_1(t_1) J_2(t_2)$$

Note that since $\int d\mathbf{x}_3 \int d\dot{\mathbf{x}}_3 P(2, 3 | 1) = P(2 | 1)$, the above fraction is the probability of ($\mathbf{x}_3, \dot{\mathbf{x}}_3$), but *not* the probability of $\dot{\mathbf{x}}_3$ given \mathbf{x}_3 .

From the definition of conditional probabilities, we can write $P(2, 3 | 1) = P(2 | 3, 1)P(3 | 1)$. Now so long as the dynamics of our particle do not involve interactions with other particles, $P(2 | 3, 1) = P(2 | 3)$ for $t_1 \leq t_3$. This is because whatever happened during $t_1 < t < t_3$ is summarized by **3**. Hence, $P(2 | 3, 1)$ does not depend on **1** so long as $t_1 < t_3$ and we can effect the following factorization:

$$\int_{t_3}^{\infty} dt_2 \int_{-\infty}^{t_3} dt_1 P(2, 3 | 1) I_1(t_1) J_2(t_2) = \int_{t_3}^{\infty} dt_2 P(2 | 3) J_2(t_2) \int_{-\infty}^{t_3} dt_1 P(3 | 1) I_1(t_1)$$

This enables us to pass at once to the case of n keypoints. Trajectories satisfying the velocity constraints connect the keypoints (including trajectories which begin and end at the same point). Thus we can write the following expression representing the fraction, $f(\mathbf{x}, \dot{\mathbf{x}})$, of particles at \mathbf{x} with velocity $\dot{\mathbf{x}}$ and which satisfy the constraints, $\{\mathbf{x}_i, \dot{\mathbf{x}}_i\}$:

$$f(\mathbf{x}, \dot{\mathbf{x}}) = S(\mathbf{x}, \dot{\mathbf{x}}) / \int d\mathbf{x} \int d\dot{\mathbf{x}} S(\mathbf{x}, \dot{\mathbf{x}})$$

where

$$S(\mathbf{x}, \dot{\mathbf{x}}) = \left(\sum_{i=1}^n M_1(\mathbf{x}, \dot{\mathbf{x}} | \mathbf{x}_i, \dot{\mathbf{x}}_i) \right) \left(\sum_{j=1}^n M_2(\mathbf{x}_j, \dot{\mathbf{x}}_j | \mathbf{x}, \dot{\mathbf{x}}) \right)$$

is the stochastic completion field of Williams and Jacobs[11] and

$$M_1(\mathbf{x}, \dot{\mathbf{x}} \mid \mathbf{x}_i, \dot{\mathbf{x}}_i) = \int_{-\infty}^{t_3} dt_1 P(\mathbf{x}, \dot{\mathbf{x}}, t_3 \mid \mathbf{x}_i, \dot{\mathbf{x}}_i, t_1) I_i(t_1)$$

$$M_2(\mathbf{x}, \dot{\mathbf{x}} \mid \mathbf{x}_j, \dot{\mathbf{x}}_j) = \int_{t_3}^{\infty} dt_2 P(\mathbf{x}_j, \dot{\mathbf{x}}_j, t_2 \mid \mathbf{x}, \dot{\mathbf{x}}, t_3) J_j(t_2)$$

represent the contributions of each keypoint to what they refer to as the *source* and *sink fields*.

Even if the I_i and J_j are time-invariant, we may wish to retain them if it should be necessary to weight the keypoints other than uniformly. As $\int d\mathbf{x} \int d\dot{\mathbf{x}} C(\mathbf{x}, \dot{\mathbf{x}})$ does not directly depend on $(\mathbf{x}, \dot{\mathbf{x}})$ (unless we need the absolute fraction) we can simply take $f(\mathbf{x}, \dot{\mathbf{x}})$ to be $C(\mathbf{x}, \dot{\mathbf{x}})$ and not worry about over-all factors (i.e., we are only concerned with the relative fraction). Furthermore, if we do not have exact knowledge of the position and velocity at the keypoints, $\{\mathbf{x}_i, \dot{\mathbf{x}}_i\}$, but instead have distributions $p_i(\dot{\mathbf{x}}_i)$ over velocity, we need only average $C(\mathbf{x}, \dot{\mathbf{x}})$ over these distributions to obtain $f(\mathbf{x}, \dot{\mathbf{x}})$.

5 Evaluation

We now turn to the evaluation of $P(2 \mid 1)$, the heart of M_1 and M_2 , where, unlike above, **1** and **2** can be arbitrary points.

$$P(2 \mid 1) = \langle \delta(\mathbf{x}(t_2) - \mathbf{x}_2) \delta(\dot{\mathbf{x}}(t_2) - \dot{\mathbf{x}}_2) \rangle_1,$$

where the average $\langle \dots \rangle_1$ is taken over-all trajectories starting at \mathbf{x}_1 with velocity $\dot{\mathbf{x}}_1$ at t_1 . Expressing the delta function as integrals:

$$P(2 \mid 1) = \int \frac{d\boldsymbol{\kappa}^d}{(2\pi)^d} e^{-i\boldsymbol{\kappa} \cdot \mathbf{x}_2} \int \frac{d\boldsymbol{\lambda}^d}{(2\pi)^d} e^{-i\boldsymbol{\lambda} \cdot \dot{\mathbf{x}}_2} \langle e^{i\boldsymbol{\kappa} \cdot \mathbf{x}(t_2)} e^{i\boldsymbol{\lambda} \cdot \dot{\mathbf{x}}(t_2)} \rangle_1$$

where d is the dimensionality of the space of interest. Thus, if one can calculate the characteristic functional

$$\Phi(\mathbf{k}_t) = \langle e^{i \int dt \mathbf{k}_t \cdot \mathbf{x}_t} \rangle_1$$

then by letting $\mathbf{k}_t = \boldsymbol{\kappa} \delta(t - t_2) - \boldsymbol{\lambda} \delta'(t - t_2)$, the expression for $P(2 | 1)$ will follow at once. Although more general cases can be treated using these methods, we will focus on trajectories of the following form:

$$\mathbf{x}(t) = -\partial_{t_1} \mathbf{G}(t, t_1) \mathbf{x}_1 + \mathbf{G}(t, t_1) \dot{\mathbf{x}}_1 + \int_{t_1}^t dt' \mathbf{G}(t, t') \mathbf{F}(t')$$

where $\mathbf{F}(t)$ is an elementary, stochastic force of dimension d . Inserting $\mathbf{x}(t)$ and $\dot{\mathbf{x}}(t)$ into $\Phi(\mathbf{k}_t)$ we find:

$$\begin{aligned} \Phi(\mathbf{k}_t) &= \exp(i \int dt \mathbf{k}_t (-\partial_{t_1} \mathbf{G}(t, t_1) \mathbf{x}_1 + \mathbf{G}(t, t_1) \dot{\mathbf{x}}_1)) \\ &= \exp(i \int dt \mathbf{l}_t (-\partial_t \partial_{t_1} \mathbf{G}(t, t_1) \mathbf{x}_1 + \partial_t \mathbf{G}(t, t_1) \dot{\mathbf{x}}_1)) < \exp(i \int dt \mathbf{p}_t \cdot \mathbf{F}_t) > \end{aligned}$$

where $\mathbf{p}_{t'} = \int_{t'} dt (\mathbf{k}_t \mathbf{G}(t, t'))$ and $\mathbf{G}(t, t) = 0$. In Appendix A we calculate $< \exp(i \int dt \mathbf{p}_t \cdot \mathbf{F}_t) >$ quite generally for \mathbf{F}_t represented as a collection of forces of various strengths and in various directions which occur at times governed by Poisson processes at time varying rates.

While we could proceed with that result, it is simplest for our purposes to take the Gaussian limit of numerous, smaller forces at constant, average rates. The result is

$$< \exp(i \int dt \mathbf{p}_t \cdot \mathbf{F}_t) > = \exp(-\frac{1}{2} \int dt \mathbf{p}_t \cdot \mathbf{T} \cdot \mathbf{p}_t)$$

which, when inserted into $\Phi(\mathbf{k}_t)$ yields for $P(2 | 1)$:

$$P(2 | 1) = \frac{\pi^d}{\sqrt{|\mathbf{P}|}} \exp(-\frac{1}{2} \mathbf{w} \cdot (\mathbf{P} + \tilde{\mathbf{P}})^{-1} \cdot \mathbf{w})$$

where \mathbf{w} is the $2d$ vector

$$\mathbf{w} = (\mathbf{x}_2 - (-\partial_{t_1} \mathbf{G}_{t_2 t_1} \mathbf{x}_1 + \mathbf{G}_{t_2 t_1} \dot{\mathbf{x}}_1), \dot{\mathbf{x}}_2 - (-\partial_{t_2} \partial_{t_1} \mathbf{G}_{t_2 t_1} \mathbf{x}_1 + \partial_{t_2} \mathbf{G}_{t_2 t_1} \dot{\mathbf{x}}_1))$$

and \mathbf{P} is the $2d \times 2d$ (block) matrix,

$$\mathbf{P} = \frac{1}{2} \int^{t_2} dt \begin{pmatrix} \mathbf{G}_{t_2 t} \\ \partial_{t_2} \mathbf{G}_{t_2 t} \end{pmatrix} \mathbf{T} \begin{pmatrix} \tilde{\mathbf{G}}_{t_2 t} \\ \partial_{t_2} \tilde{\mathbf{G}}_{t_2 t} \end{pmatrix}$$

which is readily inverted.

For our purposes, we can take the response of a free particle $G_{t,t'} = (t - t')u(t - t')$ and \mathbf{G} and \mathbf{T} diagonal. This results in

$$P(2 | 1) = P_x(2 | 1)P_y(2 | 1)\dots P_w(2 | 1)$$

where $P_r(2 | 1), r = x, y, \dots w$ correspond to the factors for each dimension. When, for example, $t_{21} = t_2 - t_1$, $x_{21} = x_2 - x_1$ and $\dot{x}_{21} = \dot{x}_2 - \dot{x}_1$, then:

$$P_x(2 | 1) = \frac{\sqrt{3}}{\pi T_x t_{21}^2} \exp\left(-\frac{6}{T_x t_{21}^3} \left((x_{21} - \frac{\dot{x}_2 + \dot{x}_1}{2} t_{21})^2 + \frac{t_{21}^2}{12} \dot{x}_{21}^2\right)\right)$$

At this level of simplification, the only remaining dimension-dependent parameter is T_r , the effective strength of the fluctuation inducing forces.

To introduce more control over the duration of the paths one can multiply $P(2 | 1)$ by a function of time $Q_{21}(t)$. When, for example, $Q_{21}(t_{21}) = \exp(-t_{21}/\tau_{21})$ then the contribution of paths of duration much longer than τ_{21} is reduced. This corresponds to letting particles decay with an average rate of $1/\tau_{21}$. Because this makes longer trajectories exponentially less likely, both Mumford[6] and Williams and Jacobs[11] employed this mechanism to model the component of the prior distribution of completion shape dependent on length. Other temporal filters $Q_{21}(t_2, t_1)$ serving alternative purposes can be used as needed.

6 Expected Trajectory

In this section, we derive analytic expressions for the expected value and variance of the completion field. This is done for arbitrary configurations of two keypoints and for trajectories of specific duration (i.e., for a given t_{21}). In Appendix B, we show how this last restriction can be relaxed (i.e., we show how the expected value and variance of the completion field can be estimated by averaging over trajectories of all durations). For the moment, we observe that the analytic expression for $\Phi(\mathbf{k}_t)$ makes it straightforward to determine the expected trajectory when t_{21} is known:

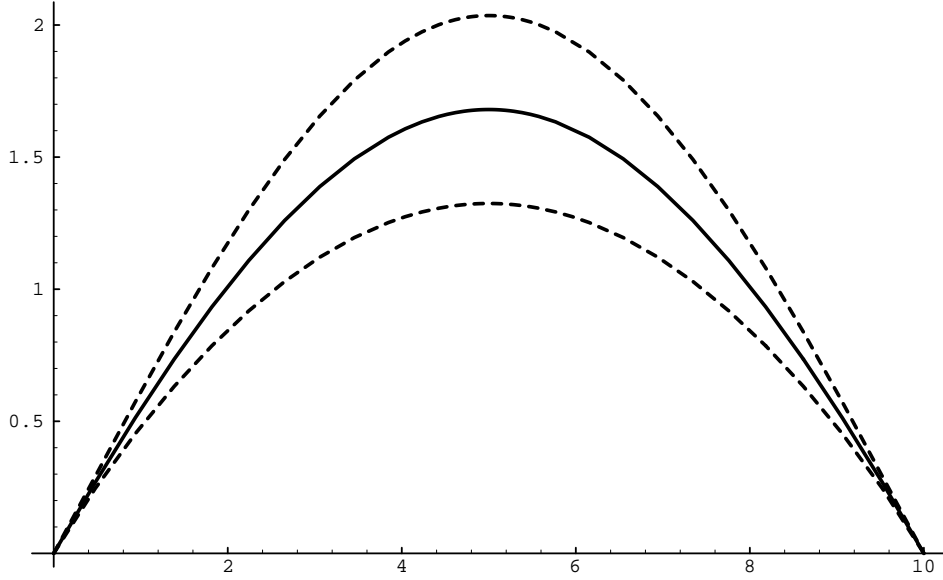


Figure 1: Expected trajectory, $\langle x_3 \rangle$, for two point configuration: $\mathbf{x}_1 = (0, 0)$, $\dot{\mathbf{x}}_1 = (\cos 30^\circ, \sin 30^\circ)$, $\mathbf{x}_2 = (10, 0)$, $\dot{\mathbf{x}}_2 = (\cos -30^\circ, \sin -30^\circ)$. Total transit time, $t_{21} = \hat{t} = 12.4$ was computed using steepest descent approximation with $T = 0.01$ (See Appendix B). Dashed lines show plus/minus standard deviation (i.e., $\pm\sqrt{(\Delta x_3)^2}$).

$$\begin{aligned} \langle \mathbf{x}_3 \rangle &= \langle \mathbf{x}_{t_3} \delta(\mathbf{x}_{t_2} - \mathbf{x}_2) \delta(\dot{\mathbf{x}}_{t_2} - \dot{\mathbf{x}}_2) \rangle_1 / \langle \delta(\mathbf{x}_{t_2} - \mathbf{x}_2) \delta(\dot{\mathbf{x}}_{t_2} - \dot{\mathbf{x}}_2) \rangle_1 \\ \langle \dot{\mathbf{x}}_3 \rangle &= \langle \dot{\mathbf{x}}_{t_3} \delta(\mathbf{x}_{t_2} - \mathbf{x}_2) \delta(\dot{\mathbf{x}}_{t_2} - \dot{\mathbf{x}}_2) \rangle_1 / \langle \delta(\mathbf{x}_{t_2} - \mathbf{x}_2) \delta(\dot{\mathbf{x}}_{t_2} - \dot{\mathbf{x}}_2) \rangle_1 \end{aligned}$$

This can be achieved in the following way:

- letting $\mathbf{k}_t = \boldsymbol{\kappa} \delta(t - t_2) + \mathbf{k}_3 \delta(t - t_3) - \boldsymbol{\lambda} \delta'(t - t_2) - \mathbf{l}_3 \delta'(t - t_3)$ in $\Phi(\mathbf{k}_t)$
- integrating over $\boldsymbol{\kappa}$ and $\boldsymbol{\lambda}$ as in the evaluation of $P(2 | 1)$
- taking $-i\partial/\partial \mathbf{k}_3$ of the result to get $\langle \mathbf{x}_3 \rangle$
- taking $-i\partial/\partial \mathbf{l}_3$ to get $\langle \dot{\mathbf{x}}_3 \rangle$.²

²Setting $\mathbf{k}_3 = 0 = \mathbf{l}_3$ following the differentiations.

The results are (letting t_{ij} indicate $t_i - t_j$):

$$\begin{aligned}
\langle \mathbf{x}_3 \rangle &= \mathbf{x}_1(t_{23}^2(t_{21} + 2t_{31})/t_{21}^3) + \dot{\mathbf{x}}_1(t_{23}^2 t_{31}/t_{21}^2) \\
&\quad + \mathbf{x}_2(t_{31}^2(t_{21} + 2t_{23})/t_{21}^3) - \dot{\mathbf{x}}_2(t_{23} t_{31}^2/t_{21}^2) \\
\langle \dot{\mathbf{x}}_3 \rangle &= 2\mathbf{x}_1(-t_{23}(t_{21} + 2t_{31}) + t_{23}^2)/t_{21}^3 + \dot{\mathbf{x}}_1(-2t_{23}t_{31} + t_{23}^2)/t_{21}^2 \\
&\quad + 2\mathbf{x}_2(t_{31}(t_{21} + 2t_{23}) - t_{31}^2)/t_{21}^3 - \dot{\mathbf{x}}_2(2t_{23}t_{31} - t_{31}^2)/t_{21}^2
\end{aligned}$$

Note that the expected value is independent of the strength of the diffusive scattering T , even though such scattering is essential if the underlying trajectories are to match $\mathbf{x}_1, \dot{\mathbf{x}}_1$ and $\mathbf{x}_2, \dot{\mathbf{x}}_2$ at t_1, t_2 . Significantly, this suggests that the method of [11] is robust to details of the stochastic process generating the completion fields. Finally, the form of the expected trajectories suggests that if one were to enforce acceleration $\ddot{\mathbf{x}}_1, \ddot{\mathbf{x}}_2$ as additional boundary conditions (e.g. to represent curvature), then the expected trajectories would involve powers of t_3 as high as the fifth, and could (almost) be written down by analogy.³

In an analogous manner to the calculation of $\langle \mathbf{x}_3 \rangle$ and $\langle \dot{\mathbf{x}}_3 \rangle$, the variance of the trajectories from these expected values can also be calculated. We find for each component

$$\begin{aligned}
(\Delta x_3)^2 &= \langle (x_3 - \langle x_3 \rangle)^2 \rangle \\
&= (T/3)(t_2 - t_3)^3(t_3 - t_1)^3/(t_2 - t_1)^3
\end{aligned}$$

Since the variance, or uncertainty, vanishes as the diffusivity T goes to zero, we conclude that the spread observed in the computed contours is due to variations in $\langle \mathbf{x} \rangle$ with the duration $(t_2 - t_1)$ of the trajectories—shorter times yield shorter contours. In order for \mathbf{x}_t to match **1** and **2**, that is, go from $\mathbf{x}_1, \dot{\mathbf{x}}_1$ at t_1 to $\mathbf{x}_2, \dot{\mathbf{x}}_2$ at t_2 , the particle must experience scattering. Ordinarily one would expect this to keep $\Delta \mathbf{x} > 0$ even for $T = 0$. Interestingly, this is evidently not the case—the uncertainty (stochasticity), instead enters from the distribution in trajectory duration. The variance of each component of the velocity, $(\Delta \dot{x})^2$, from its expected value also shows an unexpected property:

$$(\Delta \dot{x}_3)^2 = T(t_{21}^2 + 3(t_{23} - t_{31})^2)t_{23}t_{31}/4t_{21}^3$$

³Enforcing only \mathbf{x}_1 at t_1 , \mathbf{x}_2 at t_2 yields $\langle \mathbf{x}_3 \rangle = x_1 t_{23}/t_{21} + x_2 t_{31}/t_{21}$.

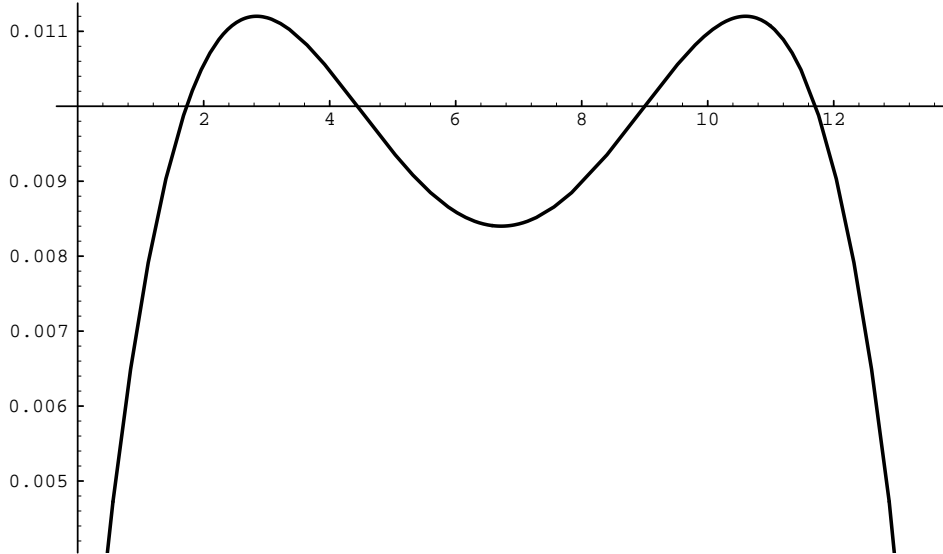


Figure 2: Variance of velocity from its expected value, $(\Delta \dot{x}_3)^2$, plotted as a function of time. Note the local minimum at mid-trajectory.

$$= T(t_2 - t_1)/16 \quad \text{for} \quad t_3 = (t_2 + t_1)/2$$

In other words, this variance has a local minimum at mid-trajectory, dropping to only one-eighth the value one would ordinarily have expected (see Figure 2).⁴ As with $(\Delta x_3)^2$, $(\Delta \dot{x}_3)^2$ also vanishes with T despite the necessity of fluctuations to match the boundary conditions.

7 Comparison w/Monte Carlo Method

In [11] the stochastic completion field was computed for a range of illusory contour figures from the visual psychology literature. This was accomplished by exploiting the fact that the stochastic completion field can be computed directly as the product of two vector-field convolutions. The convolution kernels are defined with respect to random walks beginning (or ending) at the origin with orientation zero. More specifically, the convolution kernels represent: 1) the probability that a particle beginning at $(0, 0, 0)$ will reach any other position and orientation in the image plane (i.e., (x, y, θ)) before it decays (i.e., the *source field*); and 2) the probability that a particle beginning at (x, y, θ) will reach $(0, 0, 0)$ before it decays

⁴By contrast $(\Delta x_3)^2$ is maximal at mid-trajectory.

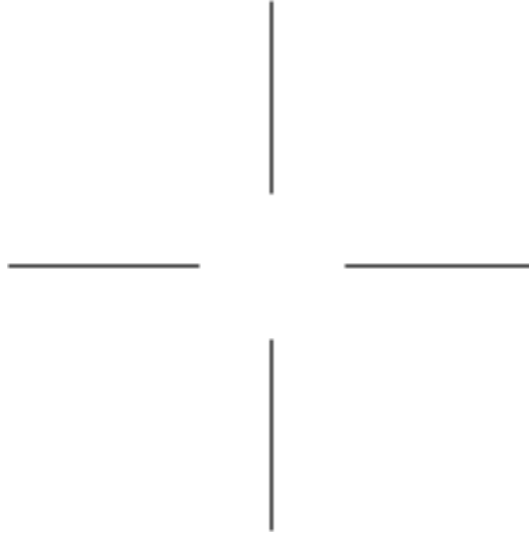


Figure 3: Ehrenstein figure.

(i.e., the *sink field*). The convolution kernels were computed by a Monte Carlo method based upon simulation of the random walk for 1.0×10^6 trials on a 256×256 grid with 36 fixed orientations. The probability that a particle beginning at $(0, 0, 0)$ will reach (x, y, θ) before it decays was approximated by the fraction of simulated trajectories beginning at $(0, 0, 0)$ which intersected the region $(x \pm 1.0, y \pm 1.0, \theta \pm \pi/72)$.

We have computed the stochastic completion field for these same figures using convolution kernels computed by setting $x_1 = 0, \dot{x}_1 = 1, y_1 = 0, \dot{y}_1 = 0, x_2 = x, \dot{x}_2 = \cos \theta, y_2 = y, \dot{y}_2 = \sin \theta$ and $t_{21} = t$ in the expression for $P(2 | 1) = P_x(2 | 1)P_y(2 | 1)$:

$$P(x, y, \theta | 0, 0, 0) = \frac{3}{\pi^2 T^2 t^4} \exp \left(-\frac{6}{T t^3} \left(x^2 + y^2 - (x(1 + \cos \theta) + y \sin \theta)t + (2 + \cos \theta)t^2/3 \right) \right)$$

and numerically integrating over the independent variable representing total transit time (i.e., t) using Simpson's method.⁵ Because the original treatment[11] used particles with a finite half-life, we used a time weighting function $Q(t)$ of the form $\exp(-t/\tau)$. In contrast with the Monte Carlo method, where it is difficult to achieve more than three significant digits of

⁵We have also approximated this integral analytically using the method of steepest descent (see Appendix B).

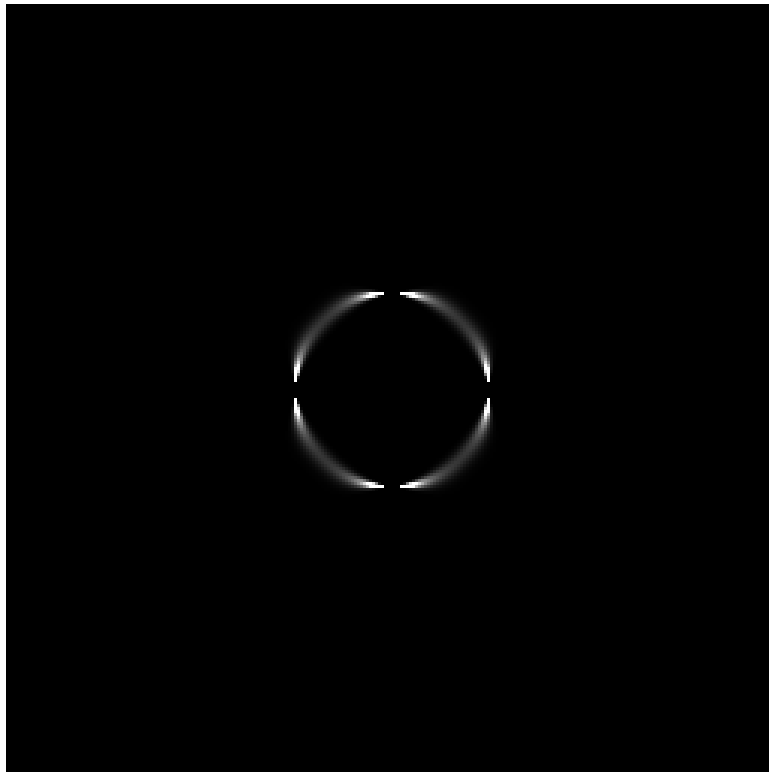
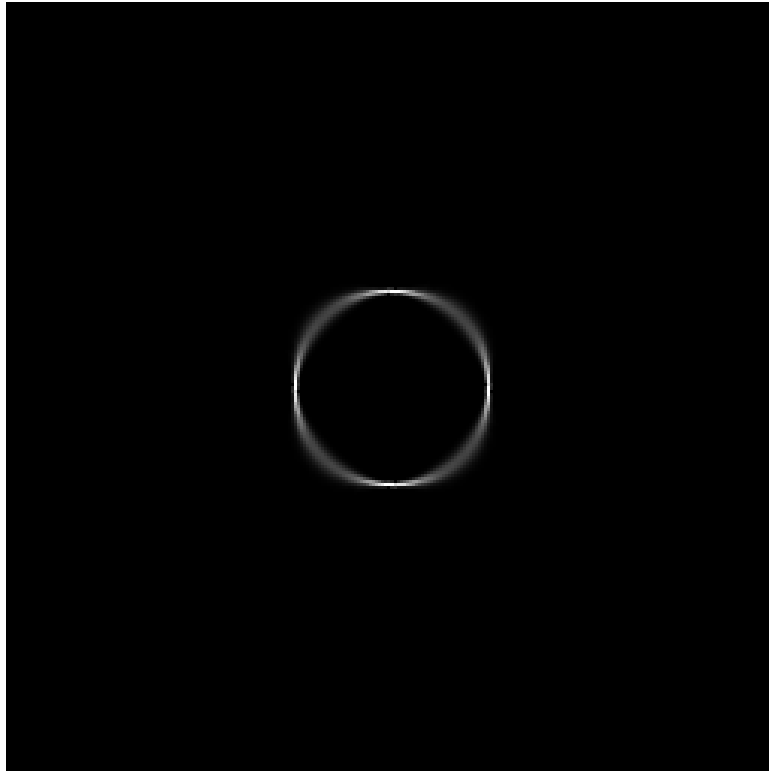


Figure 4: Top: Stochastic completion field for Ehrenstein figure computed using method of [11] (summed over all orientations). Bottom: The same, but using the filter computed by numerical integration of analytic expression for $P(2 | 1)$ instead of by Monte Carlo method.

accuracy (and this for the larger probabilities, see Section 8), the probability values computed by numerical integration of the expression for $P(2 | 1)$ are accurate to six significant digits (independent of magnitude).

As a first experimental demonstration, consider a source distribution consisting of four oriented impulses equally spaced around the circumference of a circle. This distribution is meant to represent an Ehrenstein figure (see Figure 3). The keypoints are located at endpoints of the four line segments comprising the figure and are oriented normal to the segments. Figure 4 (top) shows the stochastic completion field computed using the method of [11]. The magnitudes are summed over the 36 discrete orientations so that the stochastic completion field can be displayed as a brightness image. Figure 4 (bottom) shows the stochastic completion field computed using the convolution kernel computed by numerical integration of the expression for $P(2 | 1)$ instead of by the Monte Carlo method. The gaps in the completed figure are due to an implementation detail and are unimportant. Otherwise, there is close agreement between the results produced by each method.

The second demonstration is the well known Kanizsa triangle[5] (see Figure 5 (top)). The source distribution consisted of a set of oriented impulses representing the orientations of contours bounding regions of constant brightness at positive maxima of curvature (see [11]). In general, these are points where it is likely that one surface occludes another. Figure 5 (bottom left) shows the stochastic completion field from [11] (summed over all orientations). For illustrative purposes, it is superimposed on the brightness gradient magnitude image. Figure 5 (bottom right) shows the same, but using the filter computed by numerical integration of the analytic expression for $P(2 | 1)$.

Figure 6 (top) shows the Kanizsa “paisley” stimulus[5], which is a well known example of the *Petter effect*. The Petter effect occurs when two surfaces of equal reflectance overlap. Because the reflectances of the two surfaces are the same, their relative depth cannot be determined from figural information alone. Even so, there is a strong tendency to see the broader of the two surfaces in front of the narrower. Figure 7 (top) shows the stochastic completion field from [11] summed over all orientations and superimposed on the brightness

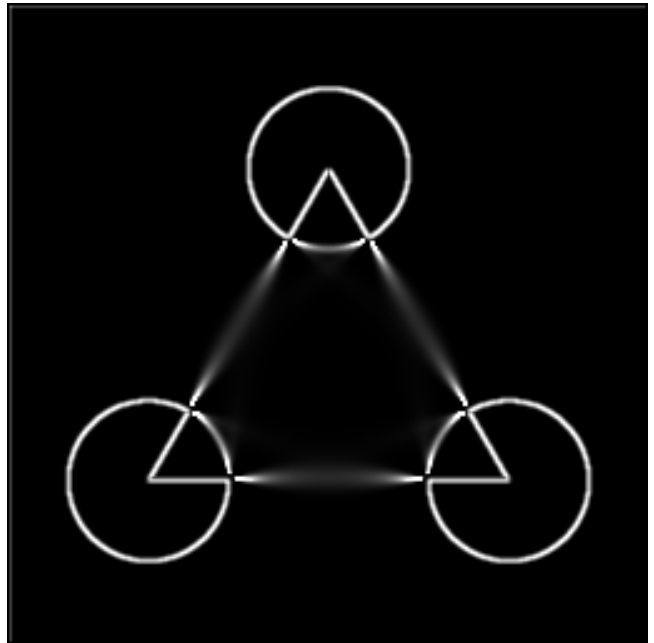
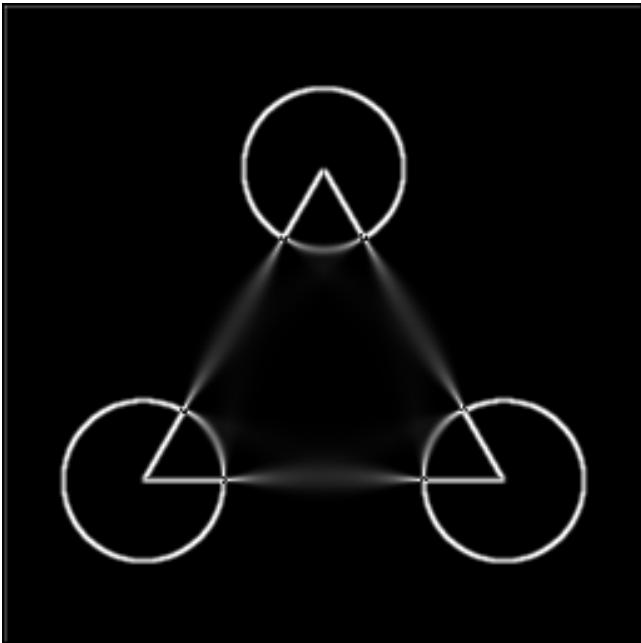
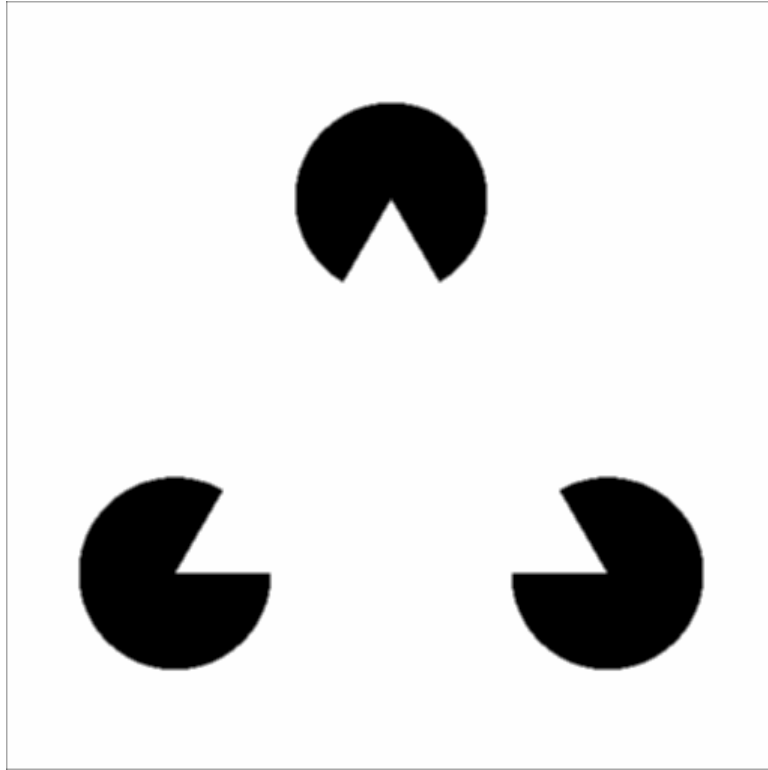


Figure 5: Top: Kanizsa triangle[5]. Bottom Left: Stochastic completion field (summed over all orientations and superimposed on brightness gradient magnitude image) from [11]. Bottom Right: The same, but using the filter computed by numerical integration of analytic expression for $P(2 | 1)$ instead of by the Monte Carlo method.

gradient magnitude image. Figure 7 (bottom) shows the same, but using the filter computed by numerical integration of the analytic expression for $P(2 | 1)$. It is interesting to note that the average likelihoods of the shorter completions are several orders of magnitude greater than the average likelihoods of the longer completions.

Figure 6 (bottom) shows a more complex illusory contour figure, also designed by Kanizsa[5]. This figure illustrates that whether or not an illusory contour is perceived is not solely a function of local configurational factors, but also depends on whether or not the completion can be incorporated in a topologically valid surface organization (see [10]). Because the diffusion process has no knowledge of the topology of surfaces, the stochastic completion field from [11] (shown in Figure 8 (top left)) contains potential completions which are not perceived by human subjects. Potential completions required to complete the four rectangles are among the most salient, however. Figure 8 (bottom left) shows the logarithm of the stochastic completion field from [11]. In the logarithm image, many additional completions of significantly lower average likelihood become visible. Included among these are those required to complete the four black discs and eight black squares perceived by human subjects. Figure 8 (top right) shows the stochastic completion field computed by numerical integration of analytic expression for $P(2 | 1)$. Figure 8 (bottom right) shows the logarithm of the stochastic completion field computed by numerical integration of analytic expression for $P(2 | 1)$. As in the other cases, there is close agreement between the results produced by each method.

8 Advantages of the Analytic Expression

Although the prohibitive amount of time required to compute the convolution kernel representing the source field by Monte Carlo methods was the original reason for turning to analytical methods, another important reason is a desire for increased accuracy. Recall that the method of Williams and Jacobs[11] exploits the fact that the completion field can be expressed as the product of source and sink fields, each of which is computable by convolution. Unfortunately, the product operation can amplify errors found in either of the constituent

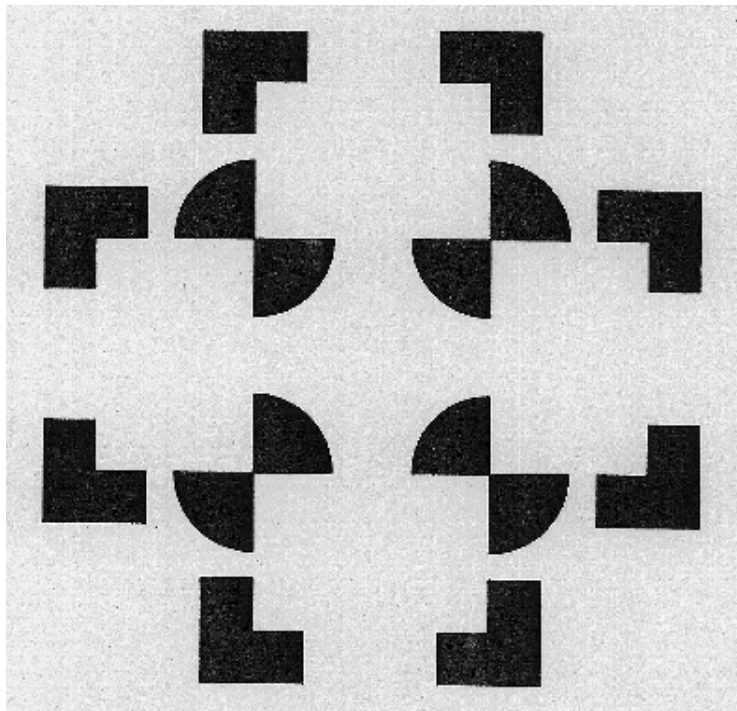
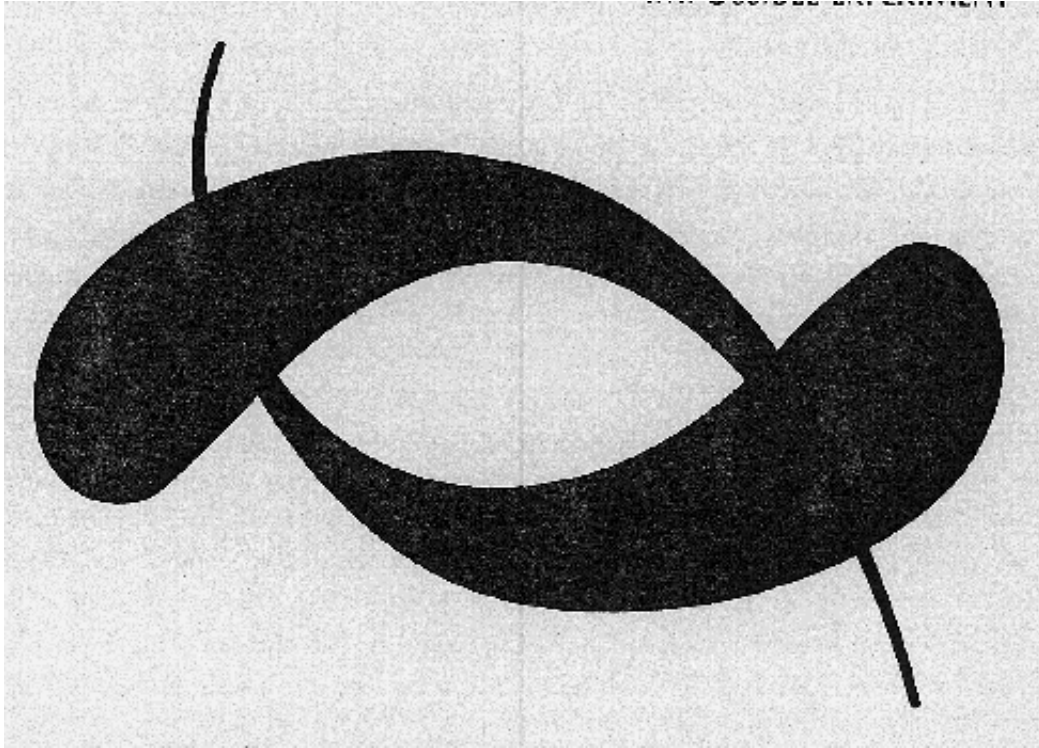


Figure 6: Top: Kanizsa's "paisley" stimulus[5]. Bottom: A complex stimulus, also due to Kanizsa[5].

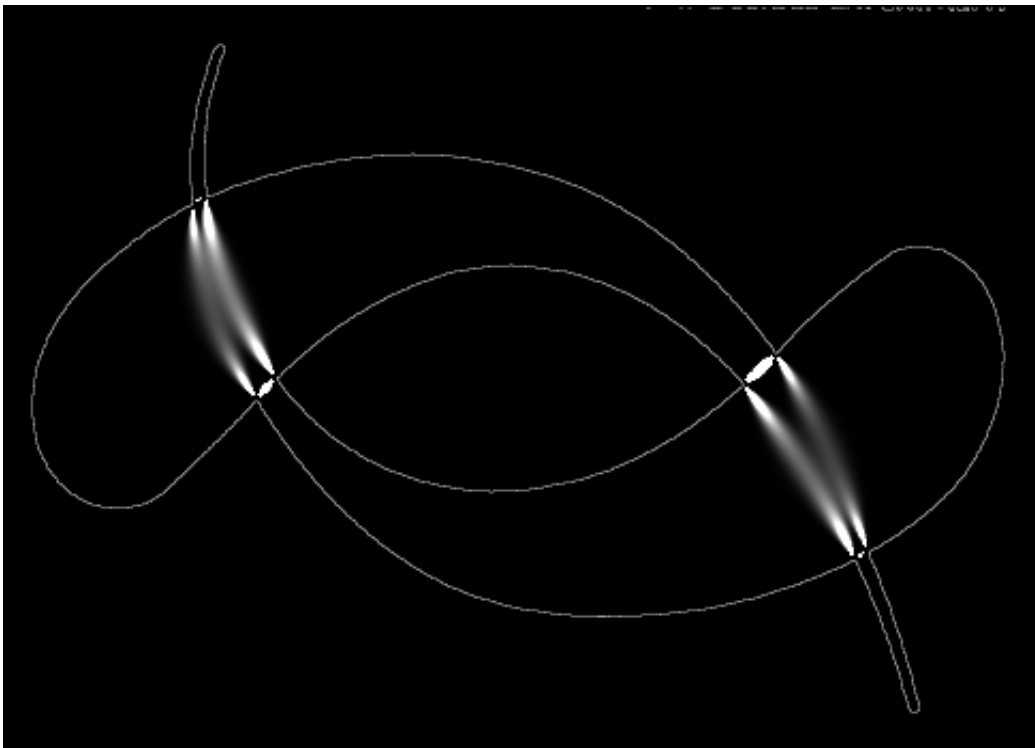
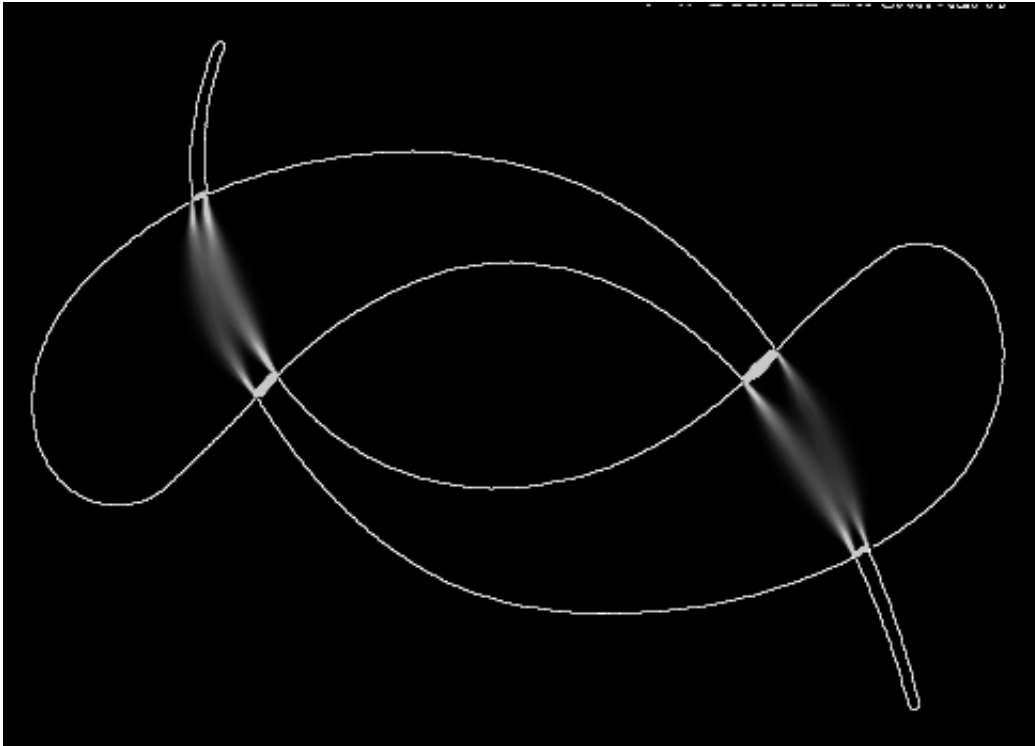


Figure 7: Top: Stochastic completion field for Kanizsa “paisley” stimulus[5] (summed over all orientations and superimposed on brightness gradient magnitude image) from [11]. Bottom: The same, but using the filter computed by numerical integration of analytic expression for $P(2 | 1)$ instead of by the Monte Carlo method.

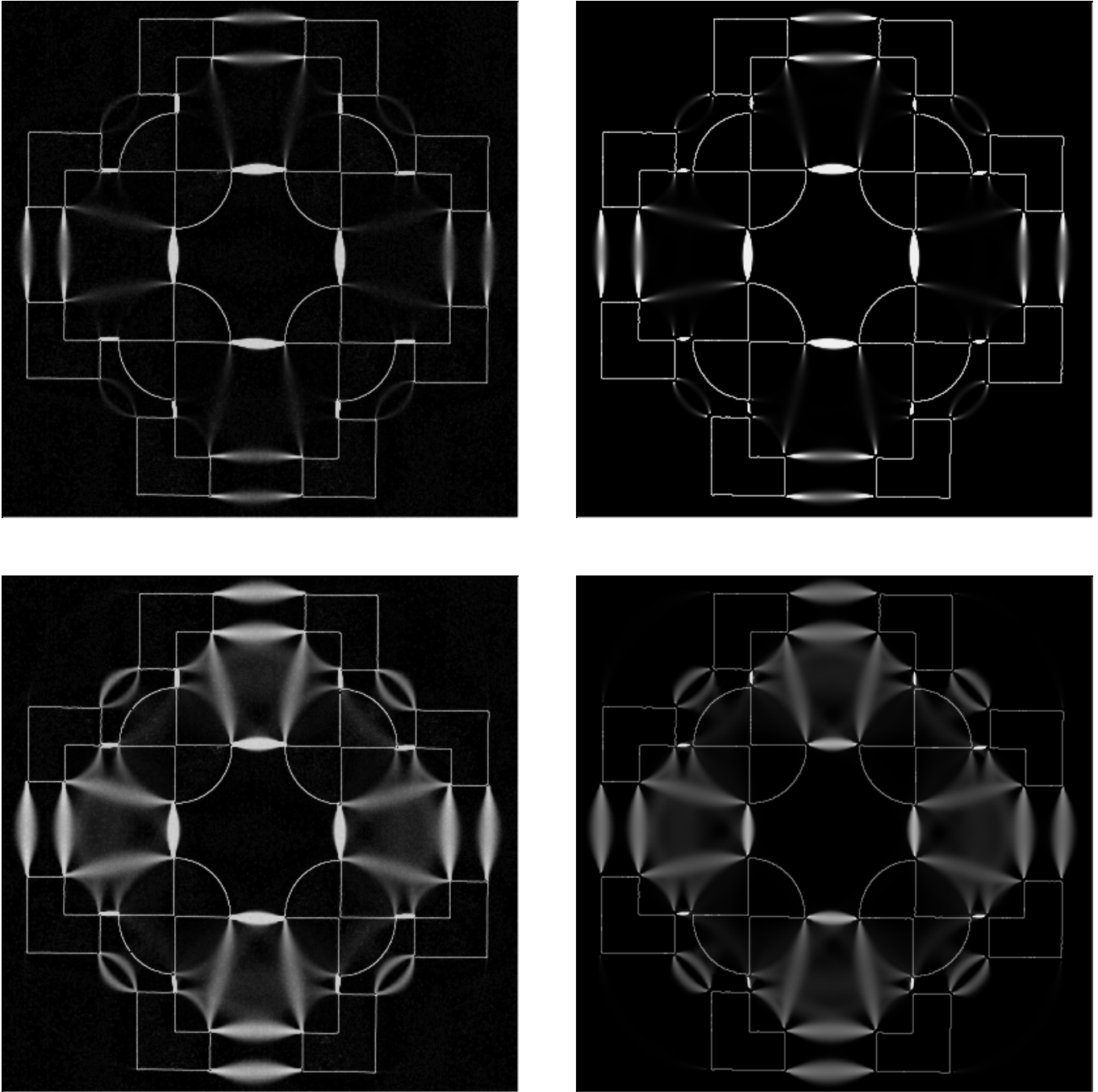


Figure 8: Top Left: Stochastic completion field (summed over all orientations and superimposed on brightness gradient magnitude image) from [11]. Top Right: The same, but using the filter computed by numerical integration of analytic expression for $P(2 | 1)$ instead of by the Monte Carlo method. Bottom Left: Logarithm of stochastic completion field (summed over all orientations) from [11]. Bottom Right: The same, but using the filter computed by numerical integration of analytic expression for $P(2 | 1)$ instead of by the Monte Carlo method.

fields. Due to the nature of Monte Carlo simulation, lower probabilities are estimated less accurately, and to increase the accuracy by a factor of two, four times as many trajectories must be simulated. The somewhat paradoxical result is that probability estimates in the largest magnitude region of the completion field (i.e., the region surrounding the expected value) can be significantly in error when the magnitude of the corresponding region of the source (or sink) field is too small. Furthermore, because the rate at which the probability magnitude of the source field drops off is a function of the variance of the distribution (i.e., the strength of the diffusive scattering), Monte Carlo methods are limited to characterizing fairly broad distributions. With the analytic solution, the accuracy of the probability estimates are percentage-wise independent of their absolute magnitude. Consequently, one can work with sharper distributions, yet achieve greater overall accuracy.

We now turn to estimating the actual errors in the Monte Carlo calculations. For a source at the origin with orientation in the direction of the positive x-axis (i.e., (0,0,0)) the source field can be estimated by a Monte-Carlo method in which Brownian particles “diffuse” in the plane, each along its own path.⁶ The fields for all other sources and sinks can be obtained from this by appropriate rotations and translations. If N is the number of paths computed and $n_{xy\theta}$ is the number of paths through the region $(x \pm dx/2, y \pm dy/2, \theta \pm d\theta/2)$ (i.e, cell (x, y, θ)), then $n_{xy\theta}/N$ for each x is the probability along a line perpendicular to the x -axis characterizing the source field:

$$\frac{n_{xy\theta}}{N} = P(x, y, \theta | 0, 0, 0) dy d\theta = P dy d\theta$$

As the root mean square (rms) fluctuations in $n_{xy\theta}$ equal $n_{xy\theta}^{1/2}$, the relative error, e of $n_{xy\theta}$ is $n_{xy\theta}^{-1/2}$ ($= n_{xy\theta}^{1/2}/n_{xy\theta}$). Thus, if too few paths pass through a cell, the estimate of the probability can be in serious error. Solving for e we find

$$e = (NP dy d\theta)^{-1/2}$$

⁶Here we assume constant speed so that only the angle θ is stochastic. If the speed were also a random variable, the error would be increased.

Not only is the number of paths we can simulate in a fixed time limited, but so is the resolution of the sampling grid. To determine ϵ , the relative error, we first observe that

$$N = \frac{t_t}{t_s} \frac{dx}{l_x}$$

where t_t is the total computer time allocatable, t_s is the computation time required to simulate each discrete time step in the Monte-Carlo runs, dx is the cell width in x and l_x is the spatial extent of the field in x .⁷ Next, taking the probability distribution to be approximately Gaussian, we have

$$Pdyd\theta = \frac{\exp(-(y - \bar{y})^2/2\Delta y^2)}{(2\pi)^{1/2}} \frac{dy}{\Delta y} \frac{\exp(-(\theta - \bar{\theta})^2/2\Delta\theta^2)}{(2\pi)^{1/2}} \frac{d\theta}{\Delta\theta}$$

where \bar{y} and $\bar{\theta}$ are the mean values and Δy and $\Delta\theta$ the rms deviations of y and θ , respectively.⁸ This is a very useful form, for it lets us estimate the probability in terms of standard deviations from the mean and element size relative to rms deviation.

For simplicity let us evaluate the above probability for $(y - \bar{y}) = k_y\Delta y$ and $(\theta - \bar{\theta}) = k_\theta\Delta\theta$ for typical values of k_y, k_θ , that is, k_y, k_θ standard deviations from the means $\bar{y}, \bar{\theta}$. Then the relative error in the source field where $y = \bar{y} \pm k_y\Delta y$ and $\theta = \bar{\theta} \pm k_\theta\Delta\theta$ is

$$\epsilon = \left(N(2\pi)^{-1} \exp(-k_y^2/2)(dy/\Delta y) \exp(-k_\theta^2/2)(d\theta/\Delta\theta) \right)^{-1/2}$$

Even for relatively large cells such that $dy/\Delta y = 1/2 = d\theta/\Delta\theta$, for $k_y = 3$ and $k_\theta = 2$ one finds that the relative error, $\epsilon = 0.12$ or 12 percent. The tradeoffs are quite apparent. Increasing the scattering will reduce the Monte-Carlo error by spreading the particles out and softening their distributions, but this will make the illusory contours more difficult to localize. Decreasing the scattering to sharpen the source field will render it more noisy in the regions most important for the formation of the completion fields. Because the completion field is the product of source and sink fields, the relative error of the completion field is the

⁷Typically $t_t \approx 3$ hours, $t_s \approx 40\mu s$, $dx = 1$ (reference length), and $l_x=256$ ($=2^8$). Thus a path takes about 10ms to execute, and $N = 10^6$ paths take about 3 hours.

⁸Here \bar{y} and Δy are functions of x , and $\bar{\theta}$ and $\Delta\theta$ are functions of y . The variances depend upon how much diffusion scattering is employed in the Monte Carlo simulation.

sum of the relative errors in each. It is not uncommon (e.g., the Ehrenstein figure), for the expected value of the completion field to be several standard deviations distant from the expected values of the source and sink fields. Unless the completion field in this region is sufficiently sharp, the illusory contour cannot be correctly localized.

9 Conclusion

In this paper, we have derived an analytic expression for the stochastic completion field. This expression is both simpler and more efficient to compute than the previously used Monte Carlo method. Most importantly, the analytic expression permits an analysis of properties of the stochastic completion field not previously possible, including expected value and variance. Significantly, the expected value of the distribution was shown to be independent of the strength of the diffusive scattering (i.e., T), depending instead on the variation in transit time (i.e., t_{21}). This suggests that the method of Williams and Jacobs[11] is robust with respect to the choice of this parameter. Finally, stochastic completion fields for a several illusory contour figures from the literature were computed using convolution kernels generated by both the Monte Carlo method and by numerical integration of the analytic expression. The results in each case are virtually indistinguishable, suggesting that the distribution has been correctly characterized.

Appendix A

Although the calculation of $\langle \exp(i \int dt \mathbf{p}_t \mathbf{F}_t) \rangle$ for nonstationary \mathbf{F}_t was carried out some time ago[7, 8], for the sake of completeness, and since the prior context was rather different (and again yet more general), we rederive it here. The key conceptual idea for stationary processes was due to Feynman[1].

If the occurrences in time of Poisson processes of mean local rates $R_k(t)$ are $\{t_{kn}\}$ (where the t_{kn} are independent) then expressing $\mathbf{F}(t)$ as

$$\mathbf{F}(t) = \sum_k \sum_{n=1}^{N_k} \mathbf{f}_k(t - t_{kn})$$

leads for $\lambda_k = \int dt_k R_k(t_k)$ at once to

$$\langle \exp(i \int dt \mathbf{p}(t) \cdot \mathbf{F}_t) \rangle = \prod_k \sum_{N_k=0}^{\infty} \frac{e^{-\lambda_k} \lambda_k^{N_k}}{N_k!} \left(\frac{\int dt_k R_k(t_k) e^{i \int dt \mathbf{p}_t \cdot \mathbf{f}_k(t-t_k)}}{\lambda_k} \right)^{N_k}$$

This follows, since in $\mathbf{F}(t)$, N_k and the $\{t_{kn}\}$ are stochastic, the N_k being distributed according to a Poisson distribution of mean λ_k and t_k can occur at random uniformly relative to $R_k(t_k)$ over any interval of interest. Carrying out the indicated sum and product we obtain:

$$\langle \exp(i \int dt \mathbf{p}(t) \cdot \mathbf{F}_t) \rangle = \exp\left(\int d\tau \sum_k R_k(\tau) (\exp(i \int dt \mathbf{p}_t \cdot \mathbf{f}_k(t-\tau)) - 1)\right)$$

Clearly this is as far as we need to go—this will give us $\Phi(\mathbf{k}_t)$ and then $P(2 | 1)$, as well as all higher-order correlation functions. However, expanding the exponent to second order in the above expression makes the characteristic functional Gaussian and enables all component integrals to be carried out explicitly. This corresponds to the limit of numerous, small random fluctuations. Should this be inadequate, one can return to the above expression. Expanding we find:

$$\langle \exp(i \int dt \mathbf{p}(t) \cdot \mathbf{F}_t) \rangle = \exp\left(- \int dt_1 \int dt_2 \mathbf{p}_{t_1} \cdot \mathbf{H}(t_1, t_2) \cdot \mathbf{p}_{t_2}\right)$$

and

$$\mathbf{H}(t_1, t_2) = \frac{1}{2} \int d\tau \sum_k R_k(\tau) \mathbf{f}_k(t_1 - \tau) \mathbf{f}_k(t_2 - \tau)$$

If the $R_k(t)$ are independent of τ , i.e., stationary, then $\mathbf{H}(t_1, t_2) = \mathbf{H}(t_2 - t_1)$.⁹ The elementary, independent, driving forces $\mathbf{f}_k(t)$ are usually taken to be of such short duration that we can write

$$\mathbf{H}(t_1, t_2) = \frac{1}{2} \sum_k R_k(t_1) \mathbf{f}_k \mathbf{f}_k \delta(t_1 - t_2)$$

Finally, for R_k stationary

$$\mathbf{H}(t_1, t_2) = \frac{1}{2} \mathbf{T} \delta(t_1 - t_2)$$

⁹The term linear in \mathbf{p}_t is usually taken to vanish, for, if it did not, it would represent a net average force on the system, which if present could be alternatively included directly in the expressions for \mathbf{x}_t and $\dot{\mathbf{x}}_t$.

and

$$\langle \exp(i \int dt \mathbf{p}_t \cdot \mathbf{F}_t) \rangle = \exp(-\frac{1}{2} \int dt \mathbf{p}_t \cdot \mathbf{T} \cdot \mathbf{p}_t)$$

This should be adequate for many cases of interest.

Appendix B

Since the integral over time $P'(2 | 1) = \int P(2 | 1) dt_{21}$ is so well behaved, it can be approximated analytically using the method of steepest descent. We wish to find \hat{t} maximizing the following:

$$-6(a/t_{21} - b/t_{21}^2 + c/3t_{21}^3)$$

where

$$a = (v_x^2 + \dot{x}_{21}^2/12)/T_x + (v_y^2 + \dot{y}_{21}^2/12)/T_y$$

$$b = 2(x_{21}v_x/T_x + y_{21}v_y/T_y)$$

$$c = 3(x_{21}^2/T_x + y_{21}^2/T_y)$$

$$v_x = (\dot{x}_1 + \dot{x}_2)/2$$

$$v_y = (\dot{y}_1 + \dot{y}_2)/2$$

The above is maximized at

$$\hat{t} = \frac{b - \sqrt{b^2 - ac}}{a}$$

yielding the approximate value for $P'(2 | 1)$ of

$$P'(2 | 1) \approx (2\pi \hat{t}^5 / 12(c - b\hat{t}))^{\frac{1}{2}} P(2 | 1)$$

where $t_{21} = \hat{t}$ in $P(2 | 1)$. This holds so long as $b^2 > ac$ and $0 < \hat{t} < t_{max}$. If $b^2 \leq ac$ or $\hat{t} < 0$ or $\hat{t} > t_{max}$ then we set $P'(2 | 1) = 0$. Finally, we note that by letting $t_{21} = \hat{t}$, $t_{31} = t$ and $t_{23} = \hat{t} - t$ in the expressions for $\langle \mathbf{x}_3 \rangle$, $\langle \dot{\mathbf{x}}_3 \rangle$, $(\Delta x_3)^2$ and $(\Delta \dot{x}_3)^2$ presented in Section 5, that we can find approximations for these values averaged over trajectories of all durations.

Acknowledgments The authors wish to thank Ingemar Cox for helpful conversations which sparked our interest in this problem.

References

- [1] Feynman, R.P. and A.R. Hibbs, *Quantum Mechanics and Path Integrals* New York; McGraw Hill, 1965.
- [2] Guy, G. and G. Medioni, Inferring Global Perceptual Contours from Local Features, *Proc. of the DARPA Image Understanding Workshop*, Washington, DC, pp. 881-892, 1993.
- [3] Heitger, R. and von der Heydt, R., A computational model of neural contour processing, figure-ground and illusory contours, *Proc. of 4th Intl. Conf. on Computer Vision*, Berlin, Germany, 1993.
- [4] Horn, B.K.P., The Curve of Least Energy, MIT AI Lab Memo No. 612, MIT, Cambridge, Mass., 1981.
- [5] Kanizsa, G., *Organization in Vision*, Praeger, New York, 1979.
- [6] Mumford, D., Elastica and Computer Vision, *Algebraic Geometry and Its Applications*, Springer-Verlag, New York, 1994.
- [7] Thornber, K.K., Treatment of Microscopic Fluctuations in Noise Theory, *BSTJ* **53**, pp. 1041-1078, 1974.
- [8] Thornber, K.K., A New Approach for Treating Fluctuations in Noise Theory, *J. Appl. Phys.* **46**, pp. 2781-2787, 1975.
- [9] Ullman, S., Filling-in the Gaps: The Shape of Subjective Contours and a Model for Their Generation, *Biological Cybernetics* **21**, pp. 1-6, 1976.
- [10] Williams, L.R., and A.R. Hanson, Perceptual Completion of Occluded Surfaces, *Proc. of IEEE Computer Vision and Pattern Recognition*, Seattle, WA, 1994.
- [11] Williams, L.R., and D.W. Jacobs, Stochastic Completion Fields: A Neural Model of Illusory Contour Shape and Saliency, *Proc. of the 5th Intl. Conf. on Computer Vision*, Cambridge, Mass., 1995.